Desalination and Water Treatment
www.deswater.com

doi:10.5004/dwt.2017.20707

73 (2017) 353–372
April

Simulation and experimental validation of Taylor-Couette flow in square cross-section container for water treatment reactor

F.Z. Sierra-Espinosa[a,*], I.A. Escamilla-Ruiz[b], Mayte L. Rodríguez[b], A. Álvarez-Gallegos[a], F. Carrillo[b], J. Teloxa[c]

[a]*Centro de Investigación en Ingeniería y Ciencias Aplicadas, CIICAp, Universidad Autónoma del Estado de Morelos (UAEM), Av. Universidad 1001, Col. Chamilpa, C.P. 62209, Cuernavaca, Morelos, México, Tel. +52 777 3297084, Fax +52 777 3297084, email: fse@uaem.mx (F.Z. Sierra-Espinosa), aalvarez@uaem.mx (A. Álvarez-Gallegos)*
[b]*Posgraduate Program Student CIICAp, UAEM Av. Universidad 1001, Col. Chamilpa, C.P. 62209, Cuernavaca, Morelos, México, email: irving.escamilla@uaem.mx (I.A. Escamilla-Ruiz), rdmayte@gmail.com (M.L. Rodríguez), fcp9@hotmail.com (F. Carrillo)*
[c]*Departamento de Ingeniería Industrial Universidad Politécnica de Tlaxcala, Av. Universidad Politécnica No. 1, San Pedro Xalcaltzinco C.P. 90180, Tepeyanco, Tlaxcala, México, email: jteloxa@uaem.mx (J. Teloxa)*

Received 8 June 2016; Accepted 15 March 2017

ABSTRACT

A vortex flow developed by a rotational cylindrical rod centrally placed in a container of square cross section was investigated experimentally and numerically. This configuration was analyzed given its potential use in water treatment. We focused the analysis on a relation of inner radius and side length $L/r = 7.33$. This ratio represents a warranty for vortex flow stability. Large ratios have the advantage of handling larger volumes with a sustained control of residence. The study was based on measuring velocity using particle image velocimetry, PIV and modelling the flow by computational fluid dynamics (CFD). Taylor-Couette cells on laminar-turbulent regimes developed for all the rotating conditions examined with Reynolds numbers between 2750 and 4950. The measurements revealed that turbulence intensity T_u increases in the radial direction towards the corners. This is by interaction fluid-walls, where corners act as natural baffles. Numerical simulations showed that secondary flows develop in the corners, with high levels of turbulence, which is important for mixing. It is shown that present configuration consumes less energy than a Taylor-Couette flow from classical concentric-cylinder systems. Heat transfer rate produced by imposed temperature conditions on the walls of the container affect vortex size and position modifying the flow structure observed in the pure dynamics case. The results indicate that configurations like square container-rotating cylinder may enhance water treatment.

Keywords: Taylor-Couetteflow; PIV velocimetry; Stirring; Square container; Thermal analysis; Turbulence intensity

1. Introduction

A reactor based on Taylor-Couette flow is important for water treatment though mixing obtained by stirring. Applications oriented to the production of microcrystals, a variety of chemical and food processes and the oil industry are feasible too. It is well known that time and quality of mixing are determinant for a successful application. Therefore, the geometry configuration of the container and the stirring mechanism play an important role. Besides, a deep understanding of the hydrodynamics involved in the process is necessary to enhance the design of the reactor from both points of view, operational cost and product´s quality.

Many mixers uses rotating propeller to stir the fluids inside a cylindrical container. However, this configuration produces very complicated flow patterns and it is very unlikely and energy consuming, it also depends on the pad-

*Corresponding author.

Presented at the EDS conference on Desalination for the Environment: Clean Water and Energy, Rome, Italy, 22–26 May 2016

dle design. Instead, investigations showed that the use of two concentric cylinders, where the inner cylinder rotates, produced good results [1]. The flow under development in concentric cylinders when one or two rotate was explained by the stability theory [2], which predicted and confirmed the experimental observation of a stable regime and its instability, made by Couette [3,4]. The transition occurs at a critical Taylor number for a rotational Reynolds number, *Re*. Inconsistences occur in limiting cases when concentric cylindrical configuration approximates to a plane flow, which is known as Couette flow. A cylindrical rotor surrounded by an external pipe flow was studied [5]. Their interest focused on the stability of an ascending flow from laminar to turbulent. They identified the excitation of Taylor vortices through the onset of the transition as function of the rotation rate. Another known mechanism that leads to flow destabilization is the effect of increasing the temperature of the outer cylinder [6,7]. It was observed that heating the inner cylinder causes a stabilizing effect while heating the outer cylinder causes the opposite effect. The case of a square enclosure with a rotating cylinder in the center, including a difference of temperatures between the lateral walls of the container, was studied [7]. Upper and lower walls were set-up as a diabatic. The mixed convective-conductive system was analyzed in terms of heat transfer as a function of the rotating rate. Particular attention was given to the analysis of the thermophysical properties of the rotating cylinder and its effect on the heat transfer process. A numerical and experimental investigation of the dynamics of Taylor vortex flow for various rotational speeds of the inner cylinder and inlet flow rates was reported [8].

Although a Taylor-Couette flow presents the characteristics of laminar regime, the geometry of the container may produce turbulent fluctuations of the velocity field. Another source of turbulence may be the presence of perturbing forces [9]. A comparison of the mixing process in a Taylor-Couette bioreactor for two *Re* numbers, demonstrated that the one with increased fluctuations of velocity produced faster mixing [10]. Therefore, turbulent kinetic energy may be important for reducing mixing times. Also, simulations of fluid stirring involving a passive scalar concentration were reported [11], in order to determine the mixing times. The impeller size was critical to the simulation mixing times. The use of modular light source (neon tubes) for biofilm cultures under controlled turbulent flowing conditions in their rotating annular bioreactor based on a Taylor-Couette type flow were investigated [12]. Non-uniform temperature was observed in the bioreactor. However, an evaluation of heat transfer rate affecting the cultures growth remains pending. It was concluded that a bioreactor based on Taylor-Couette flow is a very suitable option for investigating and understanding a variety of ecological applications related with phototrophic biofilms.

Therefore, it is clear that Taylor-Couette flow can be used for controlling a variety of processes. A vortex flow of this kind may be obtained using a rotating cylinder inside a square section container, with the benefit of managing larger volumes, based on the aspect ratio of geometry, which is larger than a concentric cylinders scheme. A large aspect ratio involves the use of less energy to achieve stable flow patterns. In concentric-cylinders a radius ratio η defined in terms of inner cylinder r_o, and outer cylinder r, $\eta = r/r_o$, determines the flow structure for a given rotation rate. Beyond the laminar and first critical value of Taylor number, an $\eta < 1.4$ produces wavy Taylor flow where vortices oscillate [13,14]. On the other hand, sufficiently large annular gaps,$\eta > 1.4$, produce vortex structures [15].

In the present work we focus the study in a relation of cylinder radius and to side length containerof $L/r = 7.33$, which represents a warranty for vortex flow stability. We analyzed experimental data and found that the interaction of vortex and flat walls increases the turbulent kinetic energy in the corners, which means that velocity is not zero in the corners. As consequence, secondary flows with ascendant descendant directions develop in the corners. This was confirmed by computational simulations. Such a large aspect ratio allows considering large in a batch or continuous operating mode with controlled residence. Also, since the size of the rotating cylinder defines the torque, it determines the total energy needed to stir the fluid. Compared against concentric cylinders systems, present configuration consumes less energy. Both, large volumes and low operating cost result attractive for a number of applications.

1.1. Comparison between the circular and cross section geometries

Table 1 summarizes sample researches on vortex motion systems ordered by type of container, stirring method, operating conditions and application. Taylor-Couette concentric cylinders reactors have been studied from the fundamental point of view, covering a wide range of operating conditions. They have been considered for multiple applications, including emulsion polymerization, synthesis of silica particles, heterogeneous catalytic reactions, liquid-liquid mixing, bio-reactions, crystallization and other continuum processes of viscous Newtonian and non-Newtonian fluids, used in food, chemical and pharmaceutical industries. As observed, the investigations vary according to the main interest of each group of researchers from pure physics descriptions to engineering parameters for a specific industrial process such as the residence time determination. However, the small capacity of volume represents a drawback for many industrial applications, except where small flow rates are possible. The variety of topics in Table 1 represent many advantages of vortex motion reactors over other reactor designs. Such wide industrial applications are enough motivation for investigating vortex flow patterns, and the search for additional enhancements such as increasing the active volume for fluid processing and reducing the power consumption in the rotor. For applications where large volumes are required, the options are cylinders and square containers with a stirrer. In this branch the kind of stirrer and the container shape define the flow path inside. It has been observed that the effects of corners may substitute the use of baffles of different kinds, which have been implemented in concentric cylinder configurations, for promoting high levels of turbulence and thus mixing. Therefore, the interest in square containers emerged. A stirrer as simple as a cylinder of small diameter combined with a square container is attractive as a bioreactor. The main motivation for investigating the present vortex motion system is UV disinfection. It is known that UV radiation does not have deep penetration into fluids like water. Vortex fluid

Table 1
Classification of applications for Taylor-Couette reactor type

Rotor-container type	Stirrer type	Operating conditions Taylor (*Ta*), Reynolds (*Re*), rotation rate (*N*)	Application	Reference
Concentric cylinder	Cylinder with helical baffles	$5.6 \times 10^6 < Ta < 3.15 \times 10^{10}$	Extraction of liquid–liquid	[16]
	Cylinder propels Rushton turbine	$0.337 < Re < 1.7 \times 10^3$	Mixing in bioprocess	[17]
	Cylinder	$1 \times 10^3 < Re < 1.5 \times 10^5$	Extraction of biological products	[18]
	Cylinder blades in bottom plate	$Ta > 1000\ Ta_c$	Liquid extraction	[19]
	Cylinder	$50 < Ta < 3.5 \times 10^4$	Tracer dispersion	[20]
	Cylinder w/without blades	$1 < Ta < 1.16 \times 10^4$	Scraped heat exchanger	[21]
	Cylinder	$Ta_c < Ta < 1000\ Ta_c$	Two-phase stratified flow	[22,23]
	Cylinder	$Ta_c < Ta < 1000\ Ta_c$	Drop size distribution	[24]
	Cylinder	$Ta_c < Ta < 1000\ Ta_c$	Two-fluid stratified flow	[25]
	Cylinder	$Ta_c < Ta < 1000\ Ta_c$	Emulsion polymerization	[26]
	Cylinder	$Ta_c < Ta < 1000\ Ta_c$	Cryst of calcium carbonate	[27]
	Cylinder	$3744 < Re < 3.7 \times 10^4$	Species reaction	[28]
	Cylinder	$Ta_c < Ta < 1000\ Ta_c$	Motor ventilation	[29]
	Cylinder	$Ta_c < Ta < 1000\ Ta_c$	Photo-catalysis	[30]
Cylinder and agitator	Propeller and vertical Baffles	$600 < N < 870$	Crystallizer for sodium bicarbonate	[31]
	Rushton turbine and vertical Baffles	$1.4 \times 10^4 < Re < 3.5 \times 10^5$	Mixing	[32]
	Propeller and vertical Baffles	$100 < N < 200$	Mixing	[33]
	Propeller and vertical Baffles	–	Aeration	[34]
Square container and agitator	Propeller	–	Aeration	[35]
	Rushton turbine	$N = 200$, $Re = 4.2 \times 10^4$	Mixing	[36]
	Propeller	$80 < N < 227$ $1.2 \times 10^4 < Re < 1.1 \times 10^5$	Flocculation	[37,38]
	Propeller	$260 < N < 517$	Mixing	[39]
	Lightnin A310 impeller	$N = 200$, $Re = 1.37 \times 10^4$	Mixing	[40]
	Propeller	N = 22.8–208.8, Re = 0.48–34.11 $\times 10^4$	Mixing	[41]

motion is expected to enhance live organisms-UV exposition by driving the streams far and close to the source of high levels of UV radiation. Compared to turbulent-laminar axial flow streams that produce conventional one direction UV bio-reactors a vortex motion flow reactor is better. The motivation for studying square containers is the high volumes compared to the narrow gap between cylinders handled in concentric cylinders systems.

2. Experimental setup

2.1. Geometry configuration

The present configuration consists of a square cross section container of length, width and useful height, *L*. A circular solid cylinder with radius, 0.06 L, was placed vertically in the center of the container, which rotates with angular velocity, *N*. The container was filled with water. Fig. 1a and 1b show side and plan views of the setup. Overall dimensions and coordinate system are included. Both, the rotating cylinder and the container were made of commercial transparent Plexiglas, of 12 mm diameter and 5 mm thickness plate, respectively. As observed, the rotating cylinder does not touch the bottom of the container. The effect of this free space on the flow dynamics was investigated by varying the distance that separates the cylinder from the bottom of the container. Additionally, this research includes other objectives, like investigating the effects of changing the diameter of the rotating cylinder, and the container aspect ratio, on the vortex motion and mixing. However, these topics will

be discussed in separate papers. Finally, the water level was 10 mm down from the top of the container.

The cylinder was driven by a DC motor equipped with a speed control mounted on the arm of a steel structure as can be seen in Fig. 1a and 1c. The accuracy of rotational speed was obtained to 0.2% by using a tachometer by Electromatic Equipment Inc.

2.2. Velocity measurements by PIV

PIV is basically a 2-D non-intrusive velocity measurement technique [42]. It has been used to study vortex motion and other complex flow structures [43–46]. The field of view in the camera is divided into interrogation areas. A plane of laser light is aligned to illuminate particles that move with the flow in the region of interest. The PIV system in this work measured the velocity field in a horizontal plane with a camera oriented from below. Both, the laser light source and the CCD camera were mounted on a 3-D traverse, which controlled the position of PIV components with a resolution of 0.1 mm with a PC. A photograph of the experimental rig can be observed in Fig. 1c.

PIV determines the displacement of particles moving with the fluid flow by projecting two pulses of laser light in order to define position one and position two of each particle. The PIV used an Nd:YAG double cavity pulsed laser beams of green light, wave length λ = 514 nm 200 mJ, with a repetition rate of 15 Hz. A Flow Sence M2/ECCD camera, of resolution 1280 × 1024 pixels, was synchronized and controlled with a BSA processor 1100 and driven using a Flow map software by Dantec Dynamics [47]. Particles of 20 μm made of silicate crystal were used to seeding the flow. A time interval Δt = 266 ms between first and second pulses of light was defined with an error of 5%, which means a level of 95% confidence from true data, from the following expression [48,49]:

$$\frac{\frac{S'}{S}\cdot\left|V_{\max}-V_{\min}\right|_{IA}\cdot\Delta t}{d_{IA}}<5\% \tag{1}$$

where $\frac{S'}{S}$ represents a magnification factor, V_{max} and V_{min} are maximum and minimum values of velocity, d_{IA} represents the length side of each interrogation area. In Eq. (1) Δt defines the initial and final position of particles on each vector field frame. A front lens by Nikon produced a magnification factor $\frac{S'}{S}$ = 7.704, for a field-of-view of 73 × 55 mm. The interrogation area size was set to 64 × 64 pixels, with 50% overlap. For most of data, the resolution in the field of view was 17.5 pixel/mm and the particle displacement was of 0.3 pixel. Velocity fluctuations were measured in this study because the stirring produced flow motions of low magnitude.

2.3. Tests conditions

Measurements of fluid velocity for rotation from N= 100 rpm to 180 rpm, with increments of 20 rpm were studied.

A period of 60 s was allowed after starting up the cylinder rotation to ensure a steady state before measuring flow

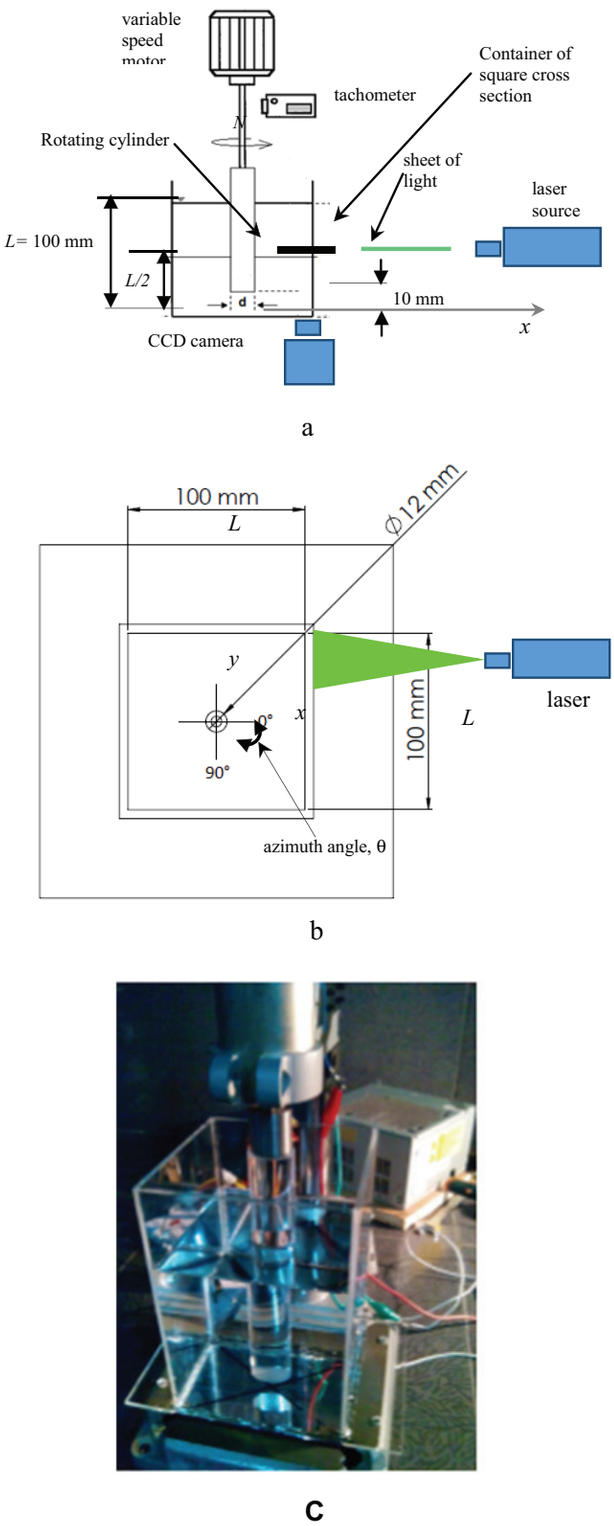

Fig. 1. Schematic description of reactor and PIV technique: (a) side view, dimensions, PIV laser, sheet of light (dotted line, on $L/2$) and camera, (b) plan view, dimensions, PIV laser sheet of light, and (c) photograph of the experimental setup.

velocity. Data from 200 images for each rotation rate were used to obtain the data time series for analysis. After each measurement, the rotating cylinder was stop and the fluid allowed to rest before starting the next run. This sequence was repeated for each rotation rate reported in this paper according to information in Table 2.

We use a parametric description for the classical concentric-cylinder system for characterizing the present cylinder-square container system, based on a rotating *Re* number [50]:

$$\mathrm{Re} = \frac{\rho\omega r\left(\frac{L}{2} - r\right)}{\mu} \tag{2}$$

where ρ, ω, and *r*, are the density, the angular velocity and the rotating cylinder radius, respectively; *L* is the length of the wall container and μ is the dynamic viscosity, and a corresponding Taylor number:

$$Ta = \frac{\rho^2\omega^2 r\left(\frac{L}{2} - r\right)^3}{\mu^2} \tag{3}$$

Re and *Ta* numbers for each run are given in Table 2. As observed in the last column of this table the Taylor number for all the experiments was for turbulent flow. By comparison to concentric cylinders systems, a classification is shown in Table 3 [51]. In the present system, the distance from the rotating cylinder to the container´s walls was assumed as the gap, analog to the gap of a concentric cylinders system. Therefore, the first critical value of Table 3, transition from Taylor-Couette to laminar Taylor flow, is defined for the present configuration for a rotation rate *N* = 0.6 rpm. Following, the transition between the laminar Taylor and the wavy vortex flows occurs at a rotation rate of 0.7 rpm.

Table 2
Conditions of experimental measurements

Test	*N* rpm	Tangential velocity, m s^{-1}	Reynolds number, *Re*	Taylor number, *Ta*
1	100	0.063	2751	5.56×10^7
2	120	0.075	3302	7.99×10^7
3	140	0.088	3852	1.088×10^8
4	160	0.101	4402	1.421×10^8
5	180	0.113	4952	1.798×10^8

Thereafter, turbulent vortex flow begins to occur at 7.2 rpm and finally no vortex or disordered flow would occur for *N* = 536.8 rpm or higher. Thus, in consequence all conditions of present configuration under analysis given in Table 2 fall on a turbulent regime.

3. Results and discussion

3.1. Effects of the azimuth angle in the horizontal plane

The flow dynamics in the plane of PIV measurements were analyzed based on time averaged velocity vector maps, such as the sample one shown in Fig. 2. When measuring, only one quarter of the total container cross section could be exposed to the source of illumination. Thus, we present one quadrant of the viewing flow field for azimuth angle $0^o \geq \theta \leq 90^o$, 0^o on *x*-axis.

As observed, the rotation direction of fluid is anti-clockwise, according to the cylinder rotation. The velocity vectors length and color scale indicate that velocity on the surface of cylinder is comparable to the magnitude of the tangential velocity of the cylinder, then it decreases in the direction of the walls of the container.

The color map indicates non-uniformities of the velocity near the cylinder's surface. These velocity variations around the cylinder are attributed to the flat walls of the container, more specifically to the corners. These velocity variations will be discussed next in terms of more detailed information through velocity profiles.

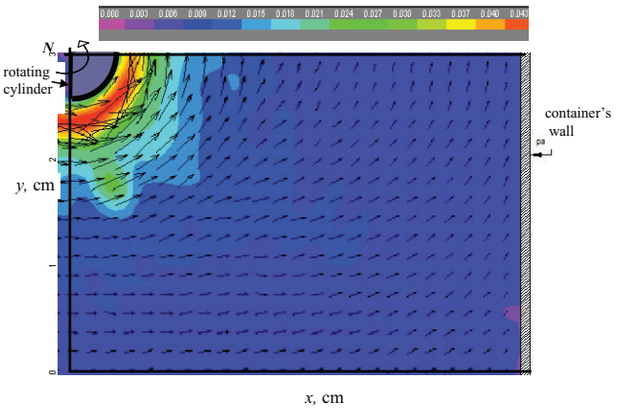

Fig. 2. PIV velocity and vectors map results for *N* = 120 rpm. Colored scale in m s^{-1}.

Table 3
Taylor number flow classification (concentric cylinder system)

Case	Ratio of radii	Taylor number, *Ta*	Flow regime	Comments
1		$0 < Ta < 1.7 \times 10^3$	Laminar	Couette
2		$Ta \approx 1.7 \times 10^3$	Transition	Taylor:Ta_c
3		$Ta > Ta_c$	Laminar	Taylor
4	<1.4	$Ta_c < Ta \approx 2.89 \times 10^5$	Transition	Wavy Taylor
5	>1.4	$2.89 \times 10^5 < Ta < 1.7 \times 10^6$	Turbulent	Turbulent Taylor
6		$Ta > 1.6 \times 10^9$	Turbulent	no vortex

3.2. Velocity profiles in the radial direction

Profiles of average velocity normalized with the tangential velocity were built in the radial direction starting on θ = 0°, where the position was normalized with the cylinder diameter starting on the cylinder surface. The results are shown in Fig. 3a–3e for all the rotation rates under study. Given the average velocity normalization, it was expected that each set of profiles for all rotation rates analyzed scales accordingly, independently of the rotation rate used.

However, by comparing the results in Fig. 3b against the rest we observed discrepancies. Maximum velocities $\frac{\overline{V}}{V_{\tan}}$ of 0.55 were obtained in this figure while $\frac{\overline{V}}{V_{\tan}}$ 0.425 are observed in Fig. 3d and 3e. The maximum average velocity also varies azimuthally up to 10%.

This reduction on the average velocity magnitude can be attributed to presence of the flat walls, and the corners formed in between, of the container. The results indicate that the lower average velocity magnitude in the vicinity of the rotating cylinder's surface corresponds azimuthally to 0°. Far from the center of the container, it was observed that the velocity falls down in the radial direction, within a radius from the cylinder surface to the container walls. In addition, the corresponding velocity profiles in the radial direction revealed that the velocity is a function of the azimuth angle, for instance for N = 120 rpm where the difference between θ = 30° and 45° is almost 20% of the maximum. Oscillations of velocity magnitude were observed for positions between y/d = 1.5 and 2.5, especially for rotation rates N = 100, 120 and 140 rpm. For N = 160 rpm the oscillations extend to the interval y/d = 1.5 and 4.5.

3.3. Comparison against concentric cylinder system

The results obtained in this work were compared against data from the literature for classical concentric cylinders Taylor-Couette flow, in order to remark the energy consumption for each configuration.

Normalized viscous torque was calculated as:

$$G = \frac{2rL_w}{2} \tag{4}$$

where τ_w is the viscous shear stress on the wall of the rotating cylinder. The results for G were plotted against the Re number as can be observed in Fig. 4a and 4b. G grows as Re increases according to [51] and [52], which occurs as well in the present results as observed in Fig. 4a. This figure extends the available data since no small relation η = r/L equal to 0.14 had been addressed before. Dimensionless torque was found to follow a power law scaling when plotted against the Re number [25], which describes also the behavior of present results observed in Fig. 5a, although a smaller magnitude of torque G was obtained here. This result was attributed to the effect of using a large gap (small ratio η = 0.14 against η = R_i/R_o, = 0.85 and 0.63 [51,52]) which means a small surface area for shear. Another cause affecting the value of G in Eq. (3) is the shear stress at the wall. In the present study τ_w changes azimuthally, because of the influence of the corners of the container on the velocity field. The effect of τ_w on the flow field is observed in the values of G, calculated from the data for the 90° azimuth, as shown in Fig. 4b. Since averaged results of G appear in the comparison of Fig. 4a, the results for 45° degree included in Fig. 4b make evident a higher effect of τ_w on the magnitude of torque in this direction. This angle corresponds with the direction from the cylinder to the corners.

Racina and Kind [26] defined the torque as the total kinetic energy dissipated in a Taylor-Couette flow, in order to keep the Taylor vortex dynamics active. However, this definition does not consider the possible effects of turbulence, which can be investigated through the structure parameters that define the level of turbulence in a flow, as it is discussed in the following section of this work.

3.4. Turbulence structure

Experimental profiles on average velocity from the plane of PIV measurement for different rotation speeds are used to extend the analysis of the flow. A classical turbulence approach, which is defined by the statistic value of stochastic velocity fluctuation, was applied from turbulence theory [53].

The first moment is the average value of the velocity fluctuations in the radial direction, u', given by:

$$\overline{u}' = \frac{1}{n}\sum_{i=1}^{n} u'_i(t) \tag{5}$$

where n is the number of data from a time series obtained directly from PIV measurements.

A turbulence intensity (Tu) was defined as:

$$Tu = \frac{rms}{\overline{u}'} \tag{6}$$

where rms is the root mean square value of the velocity given by:

$$rms = \frac{1}{n}\sum_{i=1}^{n}\sqrt{\left(u'_i - \overline{u}'\right)^2} \tag{7}$$

Eqs. (4)–(6) were equally applied to the tangential component of velocity fluctuation, v', as well. The results are presented making a comparison of velocity fluctuations in the 90° direction against the 30° data, in order to highlight the influence of flat walls on turbulence generation. It was demonstrated that any increment of turbulence means more turbulent kinetic energy can be applied for mixing [10], which applies for a Taylor-Couette bioreactor too [11].

The results of the first moment are shown in Fig. 5a and 5b, for the velocity components u' and v', respectively. Contrary to the vector velocity behavior presented in Fig. 2, the fluctuating velocity components reflect vigorous activity as function of N. The fluctuations are much more evident in the radial u' profiles compared against the tangential v' component. The results of Fig. 5a for u' indicate a difference because for an angle of 90 degree a decay is observed as the distance y/d increases, while for 30 degree the velocity presents a variable behavior. Contrary to this result, we observe in Fig. 5b a decay in the v'magnitude along the distance y/d. The variability in magnitude of the radial u' component is observed through a number of inflection points, which until the proximity of the wall. The difference of u' and v' components can be attributed to the corners; other-

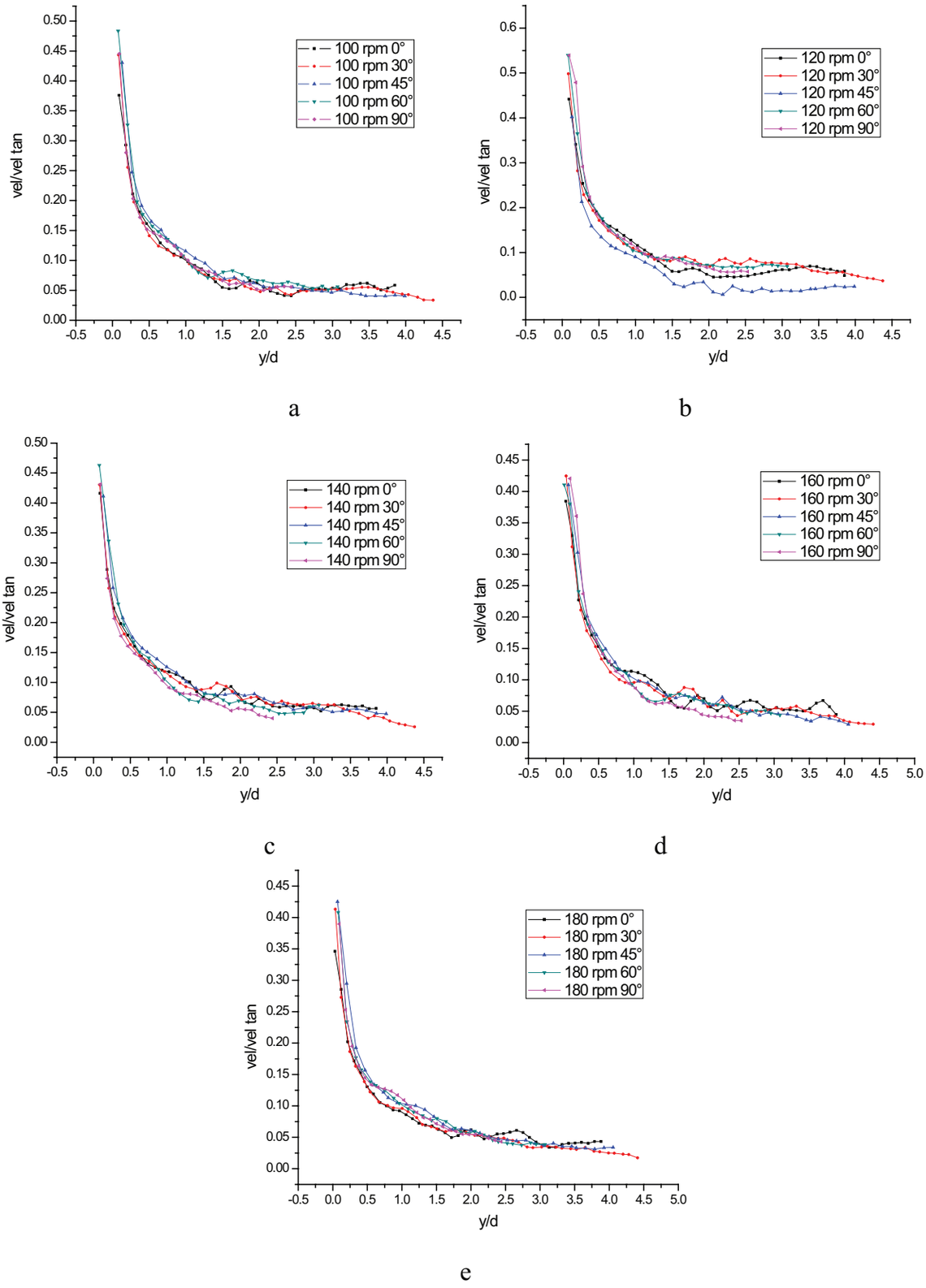

Fig. 3. Experimental profiles of average velocity in the radial direction from PIV data set: (a) N = 100 rpm, (b) N = 120 rpm, (c) N = 140 rpm, (d) N = 160 rpm, and (e) N = 180 rpm.

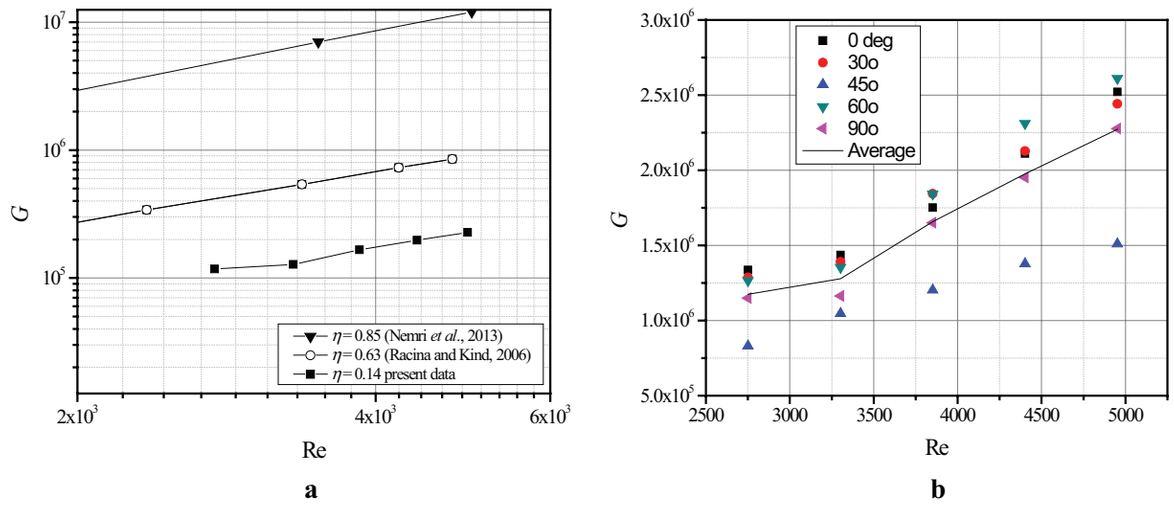

Fig. 4. Comparison of dimensionless torque from PIV data set: (a) comparison of present results against a classical concentric-cylinders system from literature data for N = 100–180 rpm and (b) dispersion from average value for present results only.

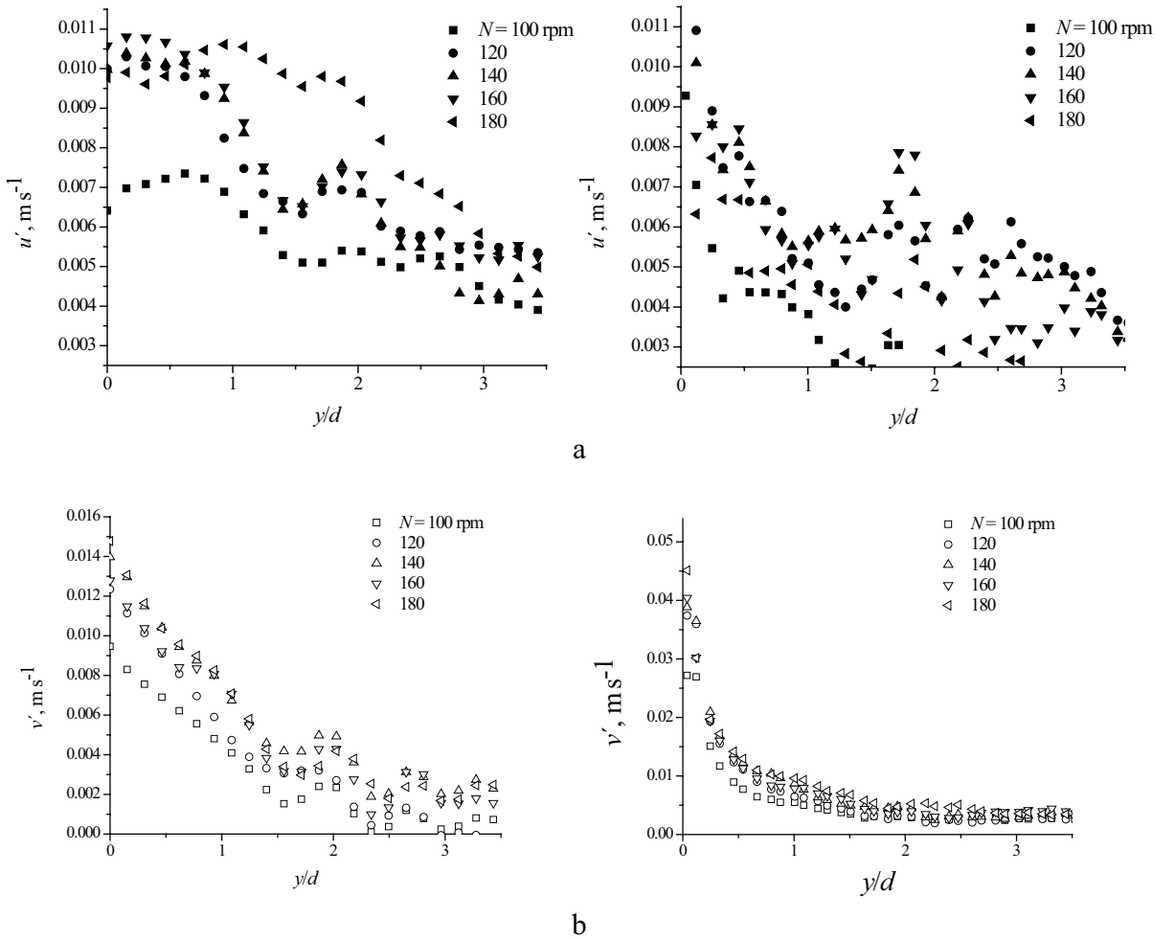

Fig. 5. Profiles of fluctuating velocity as function of distance to the cylinder for azimuth angle θ = 90° and 30°: (a) $u´$ component and (b) $v´$ component.

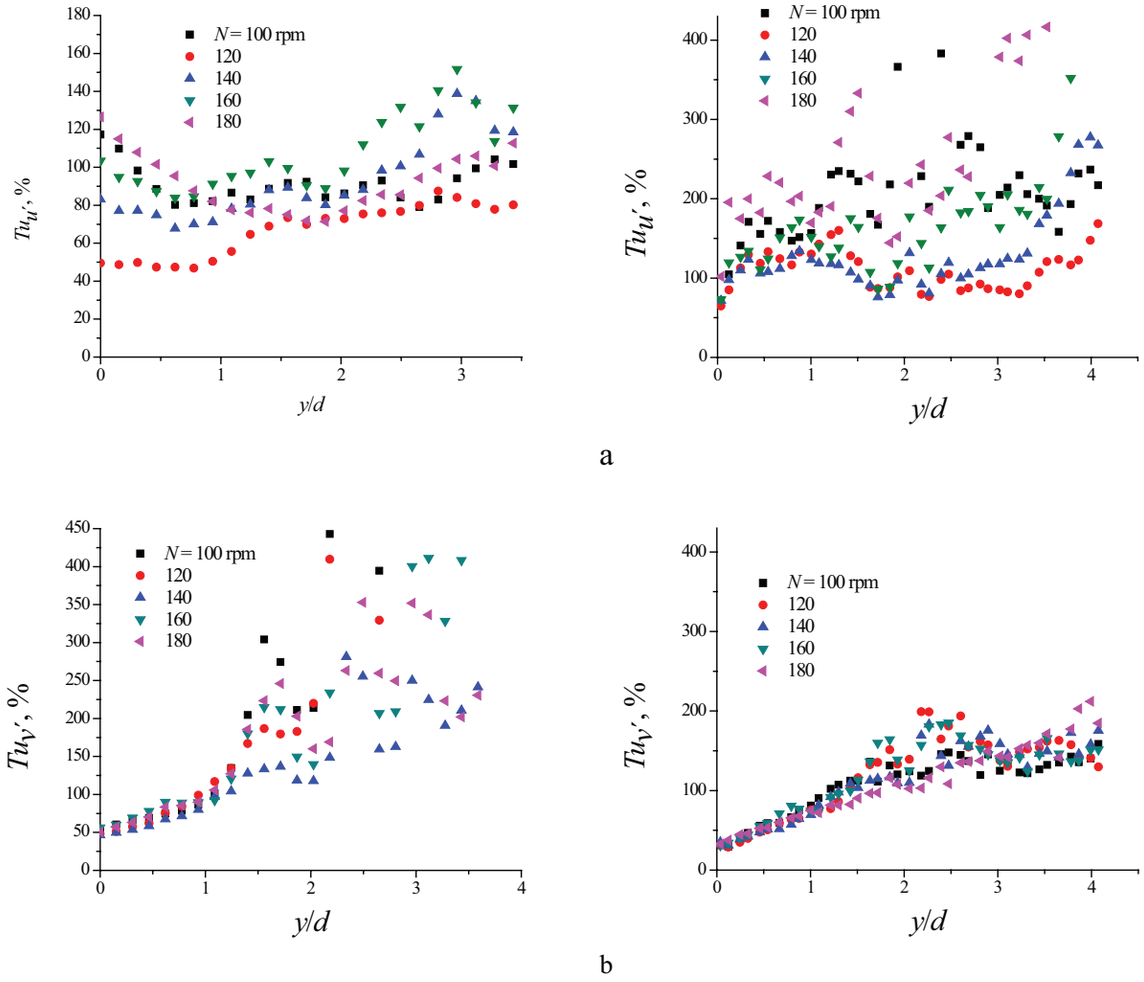

Fig. 6. Profiles of turbulence intensity *Tu* as function of distance to the cylinder for θ = 90° and 30°: (a) *Tu* of *u´* component and (b) *Tu* of *v´* component.

wise the flow pattern would be uniform, with no azimuth angle dependence.

A different scenario occurs when the turbulence is analyzed in terms of the *rms* value of the velocity fluctuation, through the turbulence intensity, *Tu*. The results of *Tu* for the *u´* component are plotted against the distance to the cylinder as shown in Fig. 6a. Instead of decaying, it is observed that the turbulence intensity increases as the distance to the cylinder increases. In this behavior of *Tu* against y/d the effect of the azimuth angle is more evident, because in the 90 degree direction, the increment of *Tu* is soft, while in the direction of 30 degree, the increment is not, except for low rotation speeds, *N* = 100 and 120 rpm. Also, a big difference is observed in the magnitude of *Tu*, since the intensity grows up to more than 400% in the 30 degree direction, while it keeps at around 100% in the 90 degree direction.

The results of *Tu* for the *v´* component are given in Fig. 6b. It is observed that the *rms* value of *v´* when normalized by the first moment produces a collapse. This collapse is stronger in the 30 degree direction compared against the 90 degree, and applies for all rotation rates. A dispersion of *Tu* starts after a distance of $y/d = 1.5$.

After analyzing the turbulence intensity of both components, *u´* and *v´*, it can be concluded that turbulence increases as function of the distance to the cylinder; as function of the azimuth angle; and finally, as a function of the rotation rate. This result is important because it represents one advantage of a cylinder-squared container from the point of view of mixing, compared against the concentric cylinder system. This characteristic behavior can be interpreted as a capability to sustain the rotating Taylor-Couette pattern and additionally, to provide extra turbulence intensity due to the flat walls.

Since the *rms* value of the velocity fluctuations was used to calculate the turbulence intensity, which increased as function of the distance to the rotating cylinder, it worth to see how it behaves when it is normalized by the friction

velocity, $u\tau$. This is because the friction velocity is based on the computation of the shear stress in the proximity of the rotating cylinder´s wall, a measure of stirring due to dynamic condition [54]:

$$u = \sqrt{\frac{\tau_w}{\rho}} \tag{8}$$

The results are shown in Fig. 7a and 7b.

In Fig. 7 it is observed that the *rms* values normalized by friction velocity collapse. The effect is so strong that the influence of the rotation condition almost vanishes. This is more evident for the direction θ = 30°, which can be understood assuming that strength of the *rms* fluctuation of velocity is due to effect of the square geometry. Compared the dynamic condition represented by $u\tau$, the *rms* value balances to unity, with peaks near the cylinder for θ = 30° and more dispersion in the direction θ = 90°. The fact that the ratio of cylinder´s diameter compared against the square side size L is small, $d/L = 0.12$, does not affect mixing since shear stress in a small region generates strong effects even far from its origin, which is confirmed by vortex motion of Taylor-Couette kind as will be show below.

4. Computational fluid dynamics (CFD) simulations

4.1. Fluid domain, grid convergence test and boundary conditions

The numerical simulations of the stirred flow by a rotating cylinder was conducted by solving the conservation equations of mass, momentum and energy. The finite volume method was employed in a commercial program [55], following the specifications for a volume of fluid VOF method. The pressure and velocity terms were linked through a SIMPLE algorithm. The turbulence was simulated employing a renormalization group theory model, RNG, within a Reynolds Averaged Navier Stokes approach, RANS. The RNG model was used because it has been tested in flows with high degree of shear with very good results [53]. The boundary conditions considered were: the velocity vanishes at all rigid walls, cylinder and container, for a no-slip condition. In VOF method the fluid surface is free of moving according to pressure conditions governed by the cylinder´s rotation. The surface of fluid was subjected to the atmospheric pressure. A 3-D computational domain was built to represent the water-cylinder-free surface configuration. An isometric of the fluid domain is shown in Fig. 8a.

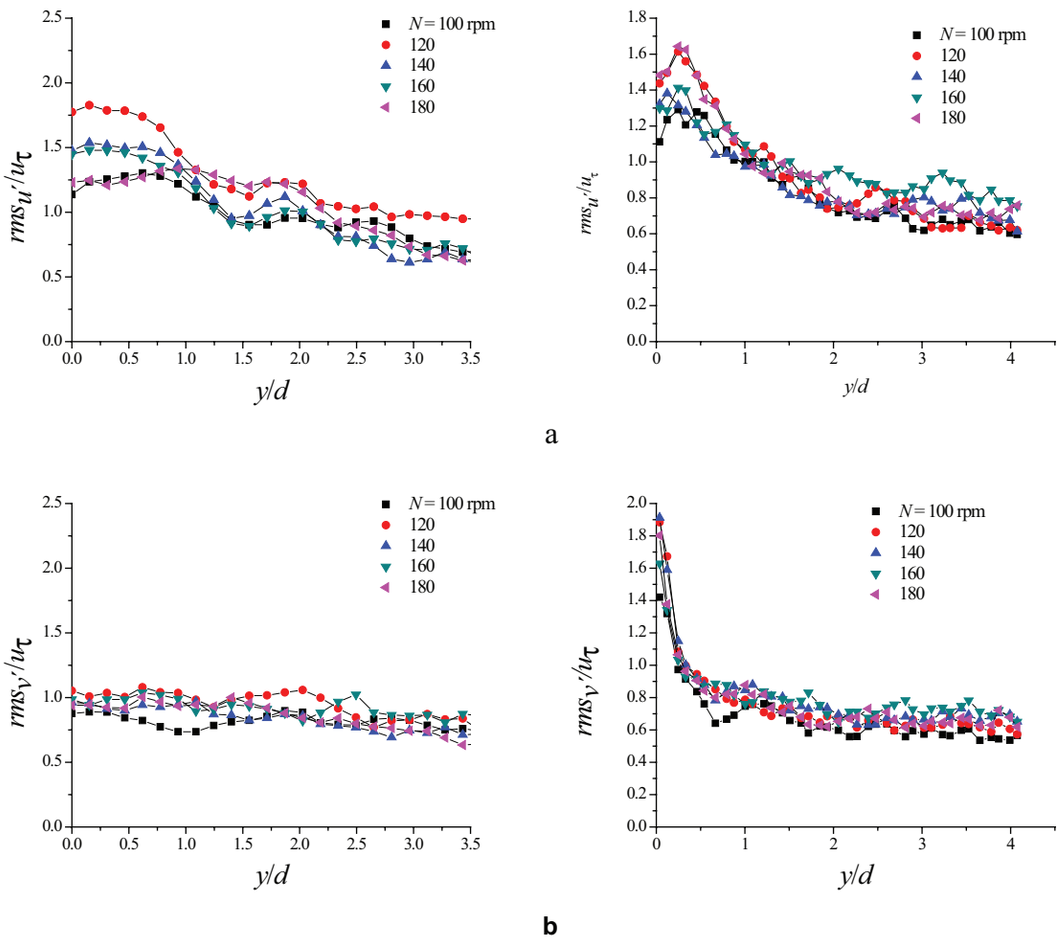

Fig. 7. *rms* values of velocity normalized by friction velocity as function of distance to the cylinder, for θ = 90° and 30°: (a) *rms* of *u´* component and (b) *rms* of *v´* component.

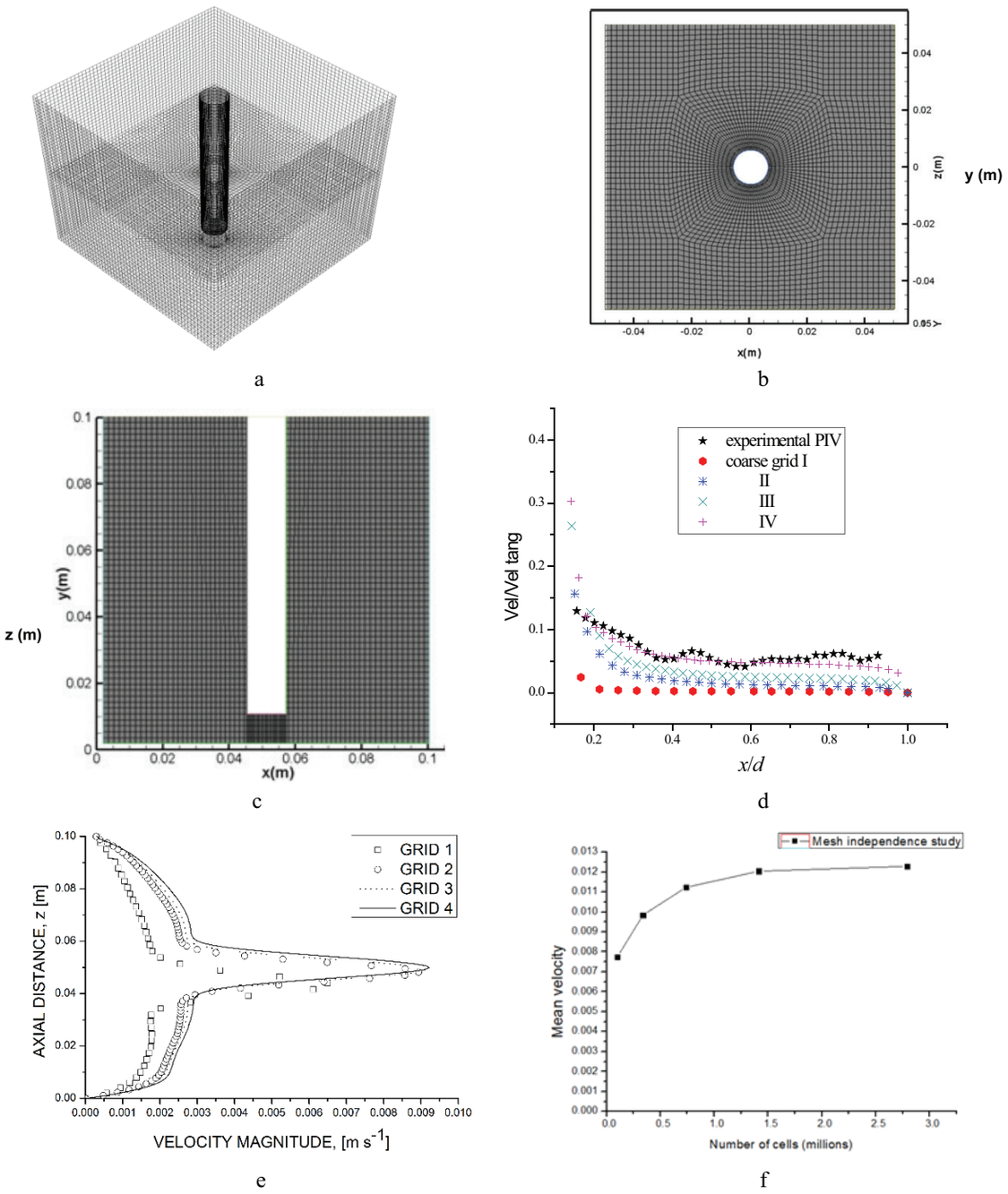

Fig. 8. Computational 3-D grid used in the simulations: (a) isometric view, (b) plan view and dimensions, (c) side view, (d) comparison of numerical profile of velocity for various grids tested against PIV experimental results for rotational rate N = 100 rpm, (e) grid convergence, velocity profile in the vertical direction, for mid-distance from cylinder to wall of container, for rotational rate N = 100 rpm, and (f) grid convergence, velocity in one central point, for mid-distance from cylinder to wall of container and surface of water, for rotational rate N = 120 rpm.

The plan view of the domain is shown in Fig. 8b, while a side view appears in Fig.8c.

The 3-D computational domain shown in Fig. 8a was divided into blocks, in order to get rectangular elements, for ease of convergence of solutions. The computational model was validated by direct comparison of the numerical results against the experimental PIV data. For proving grid independency a set of grids was tested starting with a coarse grid, following of increased number of cells grids. The results are shown in Fig. 8d with profiles of normal-

ized velocity in the radial direction. As observed in this figure, a coarse grid of less than 100,000 cells under-predicts the PIV data. However, by refining the grid to 2.8×10^6 cells the numerical profile tends to reproduce the PIV results quite close, as observed in Fig. 8d. The numerical results of velocity magnitude in the vertical direction, z, are shown in Fig. 8e. As observed, the velocity magnitude converges to no change as the grid is refined. This is also obtained for one central point as observed in Fig. 8f.

A grid independence study was carried out by calculating the grid convergence index, GCI, using velocity results, for one point located on (x = 0.028, y/y = 0.0, z/z = 0.5). The results are shown in Table 4 and were considered acceptable, since the grid independence is obtained when the value of GCI approximates 1 percent.

4.2. Description of simulation results

The numerical results in the horizontal plane for rotation rates N = 100 and 180 rpm are shown in Fig. 9a and 9b. The simulations are in agreement with the experimental PIV velocity vectors of Fig. 2. A one large-scale flow structure in the main direction of cylinder rotation is observed. However, focusing the attention on the corner for (x = 0.05, y = 0) of Fig. 9a, a vortex motion contrary to the main direction is observed. This is considered an evidence of secondary flow development in the region of the corners of the container. Secondary flows are important because they indicate that flow is not zero in the corners as commonly believed. Secondary flows in the corners will be discussed in section 4.3 by means of a 3-dimensional representation of the flow.

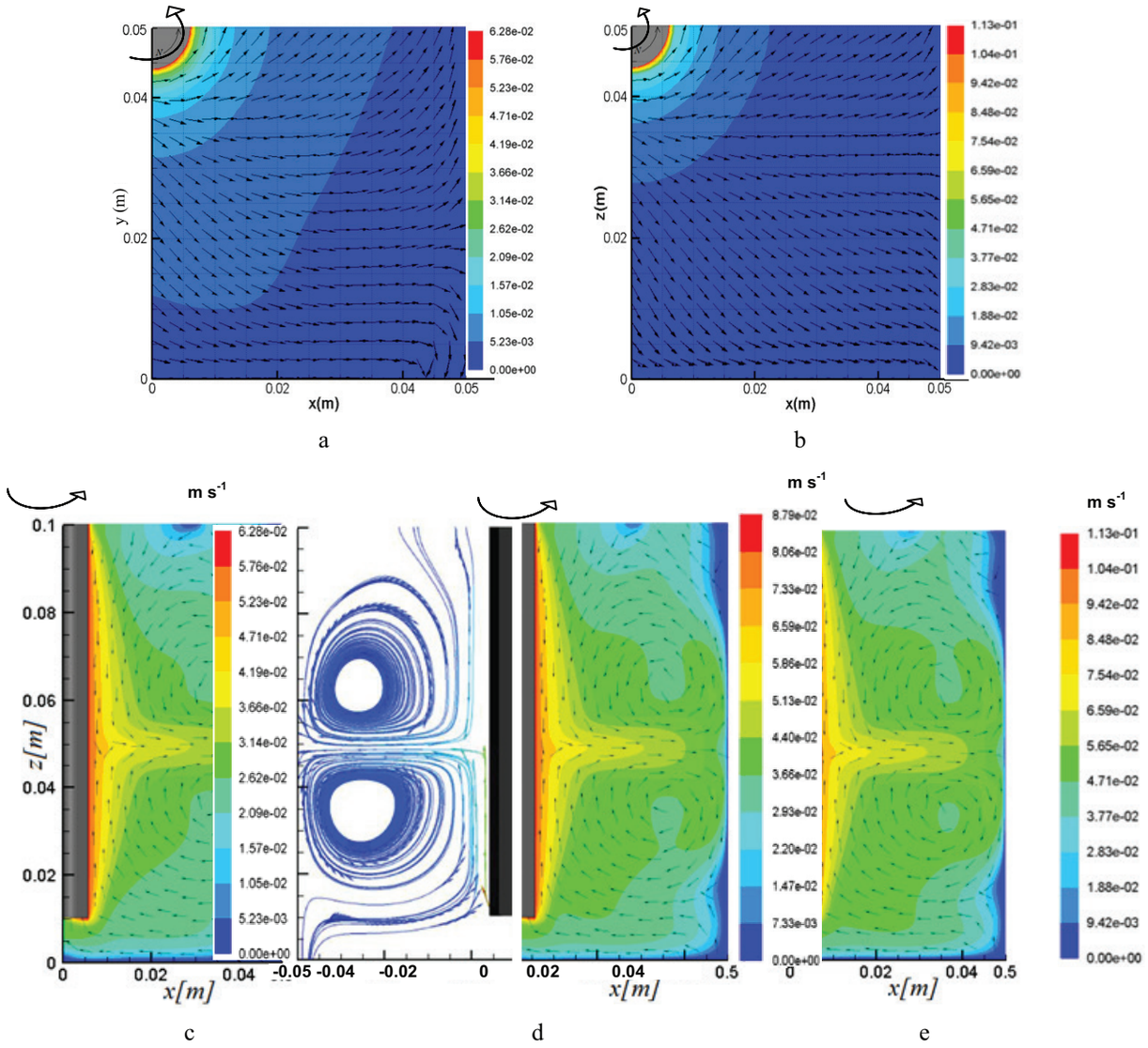

Fig. 9. Taylor-Couette flow obtained by computational results of velocity vectors maps: (a) in the horizontal plane, z = 0.05 m; N = 100 rpm, (b) horizontal plane, z = 0.05 m, N = 180 rpm, (c) half section in the vertical plane in 0° direction, N = 100 rpm, (d) full section in vertical plane in 0° direction, N = 140 rpm, and (e) half section in vertical plane in 0° direction, N = 180 rpm.

Table 4
Grid independence test data

Grid number	Number of cells	(x = 0.028, y/y = 0.0, z/z = 0.5)	Maximum volume of cell (m^3)	Size ratio, r	Grid velocity relation, ε	GCI
1	75960	0.00182	1.52×10^{-10}	–	–	–
2	738000	0.00262	0.193×10^{-10}	7.88	–0.3049	0.15×10^{-01}
3	1414000	0.0028	0.10×10^{-10}	1.93	–0.0640	0.070
4	2790000	0.00295	0.049×10^{-10}	2.03	–0.0496	0.04

The numerical velocity vectors in the vertical plane of the container complement the tri-dimensionality of the flow developed by drag effects, as observed in Fig. 9c. The vectors describe a pair of counter-rotating large-scale vortex, in the vertical plane oriented at 0° azimuth angle for N = 100 rpm. The importance of this flow structure is that a simple cylinder rotating inside a square container generates vortex motion like a Taylor-Couette flow in classical concentric cylinders systems. As in classical configurations, the gap between walls defines the size of the vortex scale. The aspect ratio height to length of the present container produce two vortex of maximum diameter equal to the gap, which deform as the rotation rate N increases.

Fig. 9a, 9b and 9c form a sequence as function of rotating rate, for N = 100 to 180 rpm. As observed, the center of vortex displaces in both x and z directions due to centrifugal force. However, the main structure is maintained for increment of rotation rate. Fig. 9d includes stream lines from the left hand side section of the container for complement the vortex size and shape.

Despite vortex deformation they indicate that symmetry is conserved with respect to the axis of rotating cylinder and with respect to horizontal mid plane. The instability of Taylor-Couette flows were analyzed and found that vortex were observed for a range of Reynolds number, but the condition at which this motion breaks-down depends on the fluid´s properties, the geometry´s aspect, and the rotation condition [54]. In the present work, all rotation rates analyzed showed vortex motion. This is because the operation range must agree with the application of water disinfection by UV radiation. The principle of this hypothesis is that the more control of vortex motion the higher the efficiency of disinfection. This is based on one fact, that all contents inside the container may be exposed to high intensity of the radiation source. This only happens for short distance to the radiation source. To this end, the location of the UV lamp is very important. The proposal is placing the radiation source inside the rotating cylinder, provided it is made of high transparency silicate crystal.

By analyzing velocity contours of Fig. 9c–9e a velocity change is detected, confirming the PIV data of Fig. 3a–3e. This variation produces a velocity gradient mainly in the region of z = 0.05 m. Two red lines placed at height z = 0.01, 0.05 m, Fig. 9d, help to define the position of the vortex structure.

According to the contours velocity maps, the fluid moves along the mid plane line with velocity in the range between 0.029 m s^{-1} and 0.007 s^{-1}, which means frequencies from 0.7 to 1 Hz, taking into account that vortex radius changes as well from initial position y/d = 1. These frequencies were identified in the time dependence data from the PIV measurements using Fast Fourier Transform analysis. The results were based on the time series shown in Fig. 10a, which represents a fluctuating flow like any other turbulent flow.

The frequencies calculated using computational fluid dynamics (CFD) predictions are in range with frequencies numbered 2 in Fig. 10b and 5 in Fig. 10c, respectively. Other frequencies correspond to secondary flows driven by vortex cells either faster or slower, but the main counter rotating cells are well defined in both results, experimental and computational.

Regarding vortex displacement in the z direction, an explanation is based on a set of 3-D views presented in Fig. 11a–11c, which were obtained through a vortex core region technique implemented in the CFD program [55].

Vortex development is out-of-phase with respect to the corners of the square container. This was observed for a rotation rate N =100 rpm as can be seen in the reconstruction 3-D view shown in Fig. 11a. In this figure, the existence of a swirling local flow pattern is visualized, as part of a developing Taylor-Couette flow. By comparing the conditions N = 100 rpm against 140 rpm 1b it is observed that distance in the vertical direction from one vortex to other decreases. While vortex orientation is in-phase with the container´s corners, in the latter case this distance is smaller. The same occurs for the maximum rotation rate investigated as shown in Fig. 11c. The sequence of figures indicates that the out-of-phase to in-phase vortex transition occurs from condition 100 to 140 rpm. The vortex motion is re-orientated to adequate the swirling pattern to the geometry configuration of the container.

4.3. Vorticity field and secondary flow

Secondary flows were visualized through vorticity fields, which were mapped with the velocity vectors in the CFD results. Fig. 12a–12c show the secondary flows, which are responsible for turbulence intensity increment *Tu* as function of the rotation rate, observed above in the profiles of Fig. 6a and 6b.

As observed in Fig. 12a–12c secondary streams are located along the corners of the container. It is evident that secondary streams represent a link between the upper and lower vortices of Taylor-Couette flow. The results indicate that this effect of secondary stream is stronger for the condition N = 100 rpm. For higher rotation they deform by contact with the walls of the container. Instability can lead to transition from one regime to another, and secondary streams may represent connection for main vortex.

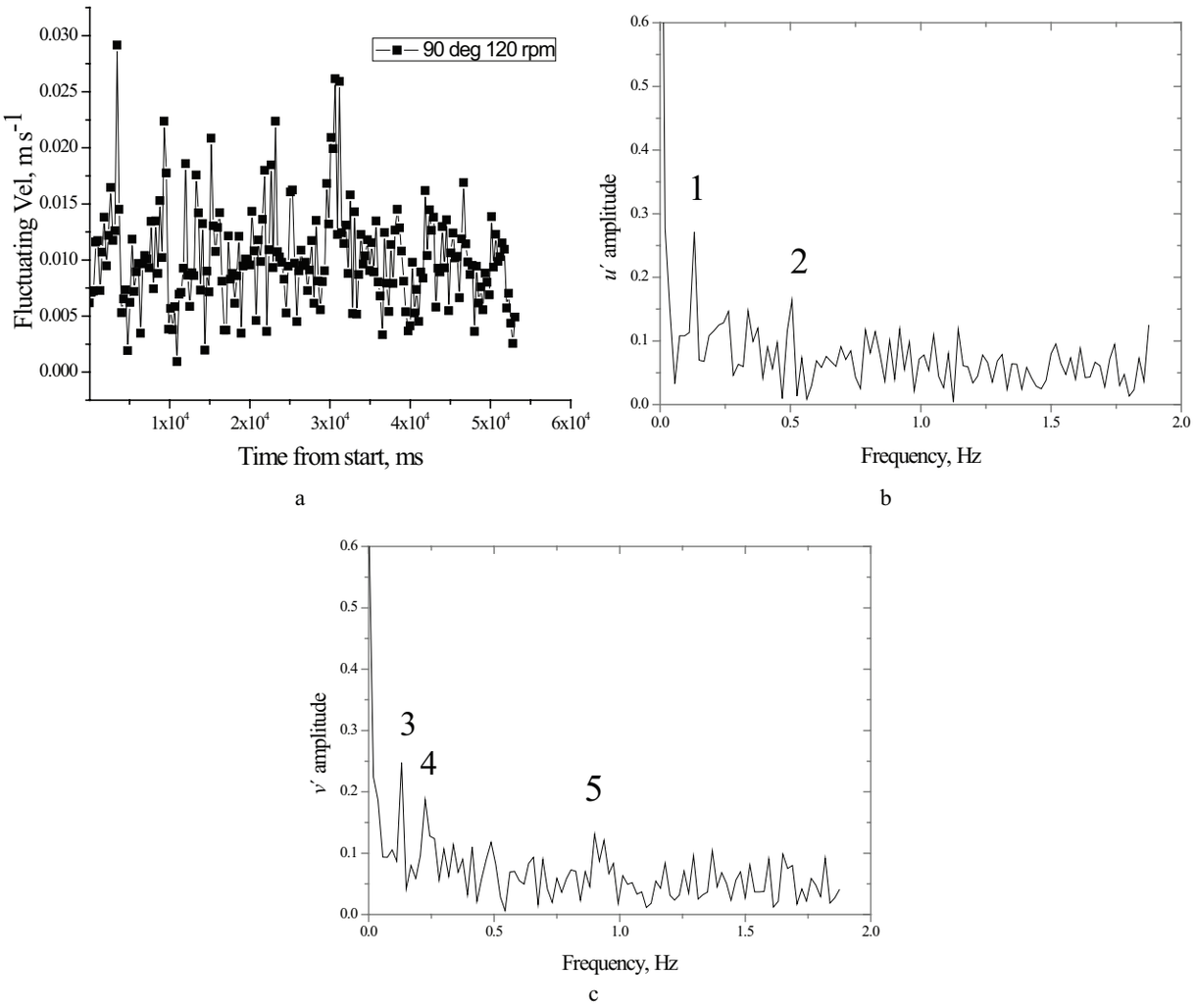

Fig. 10. Fluctuating velocity from PIV in position y/d = 1, at 90° for rotational rate N = 120 rpm: (a) time series of vector velocity, (b) FFT spectrum analysis of $u´$ velocity fluctuations, (c) FFT spectrum of $v´$velocity fluctuations. The numbers in (b) and (c) indicate the frequency of rotation of Taylor-Couette vortex, calculated from CFD results.

Secondary streams seem to originate on mid horizontal plane were vortex counter rotate. From there, streams direct in both directions, upwards and downwards, with increased size and momentum. This result was confirmed by a secondary flow rotating in clockwise direction observed in the horizontal plane shown in Fig. 9a. It may be concluded that momentum and mass transfer occurs between Taylor-Couette vortex through these corner secondary streams. Intra-vortex mixing, which means interchange of mass and momentum from one vortex to another, has been reported recently for classical concentric cylinders Taylor-Couette reactors operated on continuous mode [14]. However, no mechanism like secondary flows of Fig. 12 has yet been identified. This result suggests that momentum and mass transfer balances through a process driven by centrally upwards-downwards-flow streams, which form part of the large-scale vortex.

The effect of Taylor vortex on processes like crystallization depends on the rotation speed of the inner cylinder in addition to the feed concentration and the feed flow rate [13], but the results in Fig. 12 indicate that secondary streams may play a main role as a mechanism for enhanced mixing processes. Therefore, by controlling the cylinder rotation rate the effects of vortex transition and turbulence on crystal growth can be minimized.

4.4. Thermal analysis

Temperature distribution in the fluid was analyzed given the importance of heat transfer in many industrial applications like crystal growth [13]. The thermal-dynamics simulation assumed a Newtonian, incompressible fluid, with the application of boundary conditions as follows: at walls, temperature $T = T_w$; otherwise, the adiabatic condition applies, $\partial q/\partial z = 0$. At fluid interior, temperature $T = T_0$. At fluid surface, the ambient temperature is applied, $T_a = T_0 = 300$ K. T_w was fixed on one or two walls while the

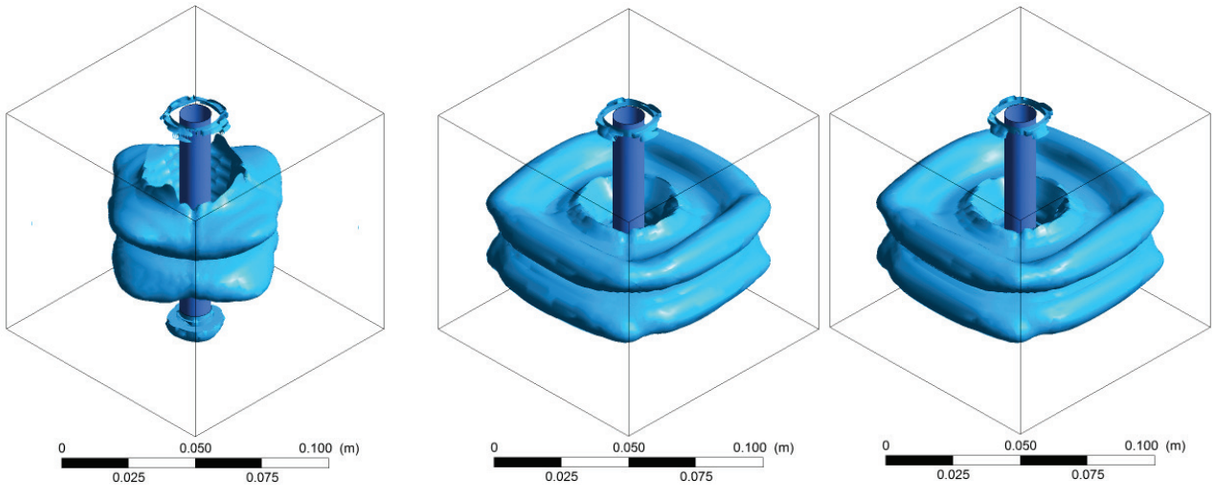

Fig. 11 Vortex core representation as isometric view of 3-D from CFD simulations: (a) Swirl strength for N = 100 rpm condition, (b) N = 140 rpm, and (c) N = 180 rpm.

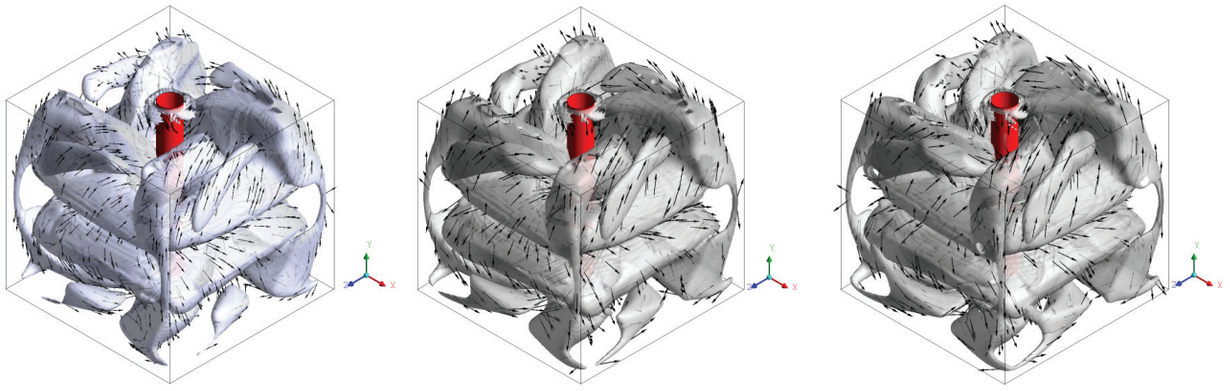

Fig. 12. Secondary flows linked to vortex in isometric view of 3-D flow from CFD simulations mapped with velocity contours: (a) Swirl strength for N = 100 rpm condition, (b) N = 140 rpm, and (c) N = 180 rpm.

rest were considered as adiabatic walls. The fluid temperature was initially T_0 = 300 K. While walls were heated three cases were considered, called *Tb*, *Tp* and *Te*. In these cases T_w varied from 310 K to 330 K with increments of 5 degree. A schematic view of each case under study is presented in Figs. 13a, 14 b and 14 c.

Heating conditions of Fig. 13 are based on usual processes like the Czochralzki method [13]. Steady state results for N = 100 rpm and *Tb* = *Tp* = *Te* = 310 K are presented in Fig. 14a–14 c in the form of stream lines and temperature maps on one vertical plane that cuts the container by middle. The results show Taylor-Couette vortex flow even under heating conditions imposed on one or two walls. The effects of heating are: Vortex structure becomes deformed as observed in stream lines of Fig. 14 compared against the pure dynamics results given in Fig. 10d. This deformation occurs in the upper vortex, which elongates in the horizontal direction while the lower vortex remains with circular shape. The vertex of upper vortex changed position moving towards the center of the container. Deformation of vortex is due to buoyancy resulting from heating, which is ascendant. A resultant of buoyancy-centrifuge forces points out diagonally, which is observed in the streamlines of Fig.14.

The maps of temperature in Fig. 14a–14c, indicate that heat diffuses through the central region in the case bottom heating. Instead, balanced heat transfer occurs when lateral heating is applied. The central region represents an obstacle for heating given the presence of the cylinder. However, below the cylinder a suction zone eases heat diffusion as observed in Fig. 14a. Furthermore, the influence of this suction zone defines a well heated central zone in the case of double-wall heating, Fig. 14c. Instead, while the surface of fluid is kept at ambient temperature, heat diffused until reaching the surface is lost to the ambient. Thus, heating is very slow towards the upper region, which is observed in all three figures.

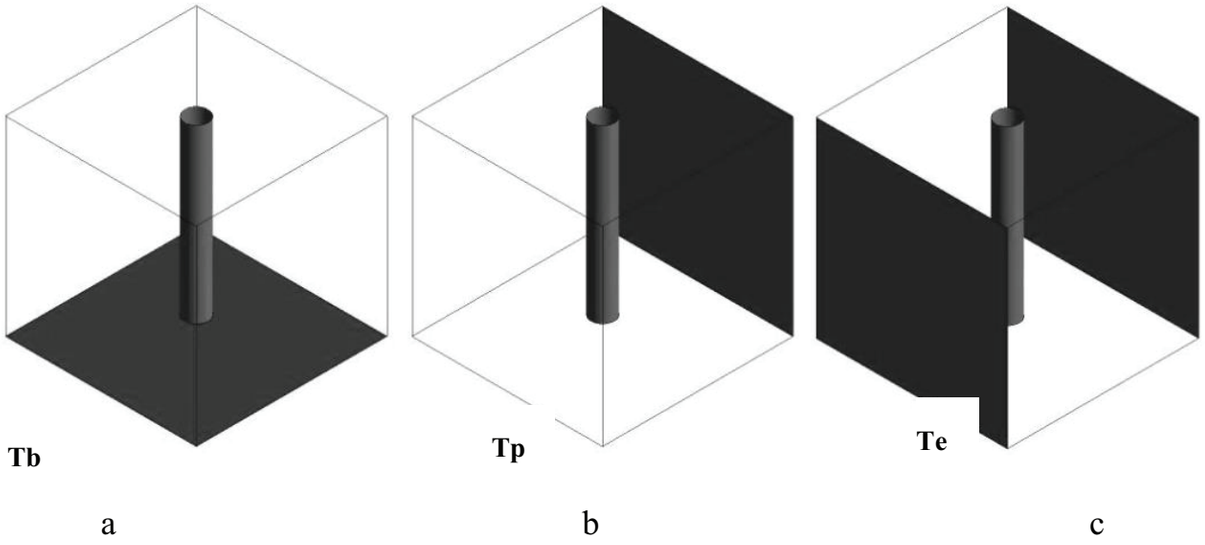

Fig. 13. Boundary conditions applied in the CFD heat transfer simulations: (a) heating on the bottom, (b) heating on one side wall, and (c) heating on two side walls.

The maps of temperature in Fig. 14a–14c, indicate that heat diffusion balances throughout the whole container, since a large portion of space in the upper region remains at low temperature. The temperature remains at low level mainly in the case bottom heating, which produces two well defined heating regions: cold in the top and hot in the bottom (see Fig. 14a). This result is consistent with the influence of the water surface condition on the top of the container, which is maintained at ambient condition.

Another thermal result in the lower region of the container is that the thermal symmetry is broken in the vertical direction. This result was confirmed by an insight into the horizontal plane at mid height for the three cases under study, which are shown in Fig. 15a–15c. In the case of heating the bottom, the temperature at mid height remains almost unaltered in the whole cross section, as observed in Fig. 15a. Instead, the temperature rises to the mid plane when heating is imposed on one or two lateral walls, as observed in Fig. 15b and 15c. By imposing the heating condition on two lateral walls, symmetry is observed in the x direction, see Fig. 15c. Heat transfer due to convection leads to almost uniform temperature. However, when heating on one lateral wall, Fig. 15b, the temperature map shows also that there is no more symmetry in the horizontal direction.

An explanation for this lack of symmetry in the horizontal direction is that heating was not imposed in the four walls. However, an important result is the thermal stratification, which means density stratification. Since density is involved in a mixing process, the lower region of the container may represent a good control for temperature. The results can be interpreted as two well mixed regions with the interface in the middle height defined by the dimensions of the upper and lower vortex. The temperature distribution in the container was analyzed also by plotting profiles along the z coordinate from the bottom to the top surface, for position x = 0.02 m. The results are shown in Fig. 16a–16c, for all three cases studied.

An inflexion point is observed for all cases located near z/H = 0.4, which indicates the position of the interface between the upper and lower vortex. The inflexion point displaces slightly only for cases of lateral heating: *Tp*, and more for case *Te* because the wall temperature increases.

The inflexion point is more pronounced in the cases of heating the bottom and two walls. Fig. 16a, bottom heating, confirms that heat diffuses with difficulty because high temperature reaches up to a zone located on z/H = 0.1, the suction zone; afterwards it falls down from the inflexion point on. On the contrary, when heating is imposed in one and two lateral walls heating is almost uniform.

Nusselt (*Nu*) represents a measure of convection heat transfer occuring at any surface. Therefore, it is worth to analyze *Nu* in order to highlight the effects of cylinder rotation, included in the Reynolds number, *Re*. Profiles of *Nu* number in positions at midheight H/2, at (x = 0.025, y = 0.025) for bottom heating, and at (x = 0.1 m, y = 0.05 m) for lateral wall heating, plotted against the rotation Reynolds number over the whole range of heating, are discussed. The results are shown in Fig. 17a–17c.

It is observed that as the Reynolds number increases *Nu* increases as well, for all temperatures of heating, and for all three heating cases. However, we observe that the wall bottom heating case, Fig. 17a, produces the lower *Nu* rates, while maximum *Nu* rate belongs to heating two lateral walls.

By analyzing the Nu number slope in the profiles of Fig. 17a–17c, it is observed that heat transfer between fluid and container lateral walls is larger for bottom heating compared against lateral heating. This means that *Nu* increases faster as the rotation rate increase for the case of bottom heating compared against lateral heating.

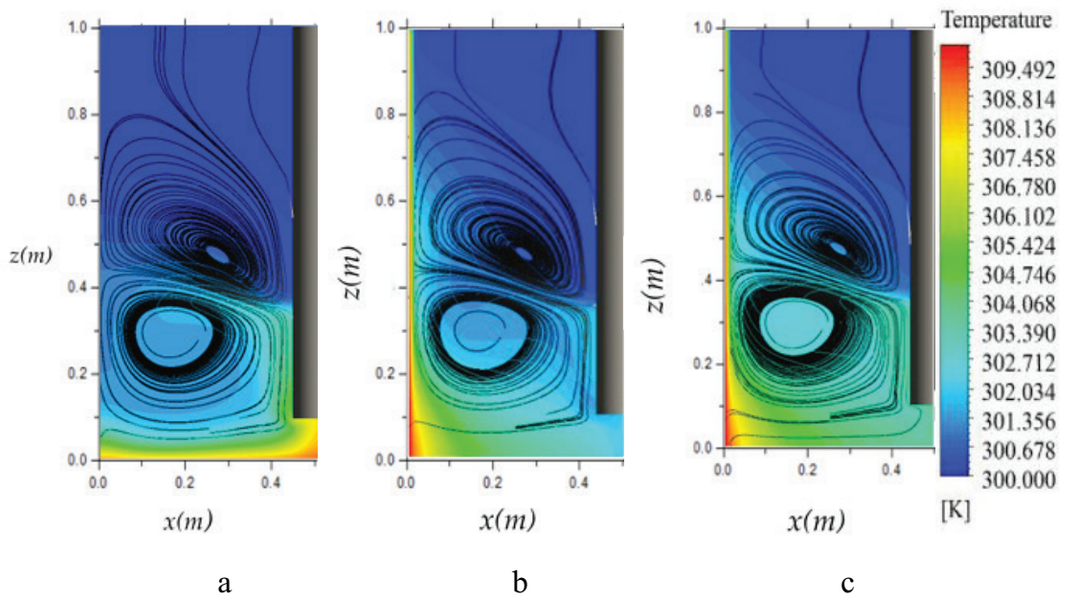

Fig. 14. Thermal dynamics results in the vertical plane in the form of temperature contours and stream lines for studied heating conditions, rotation N = 100 rpm: (a) bottom heating, Tb = 310 K , (b) one lateral wall heating, Tp = 310 K, and (c) two lateral walls heating, Te = 310 K.

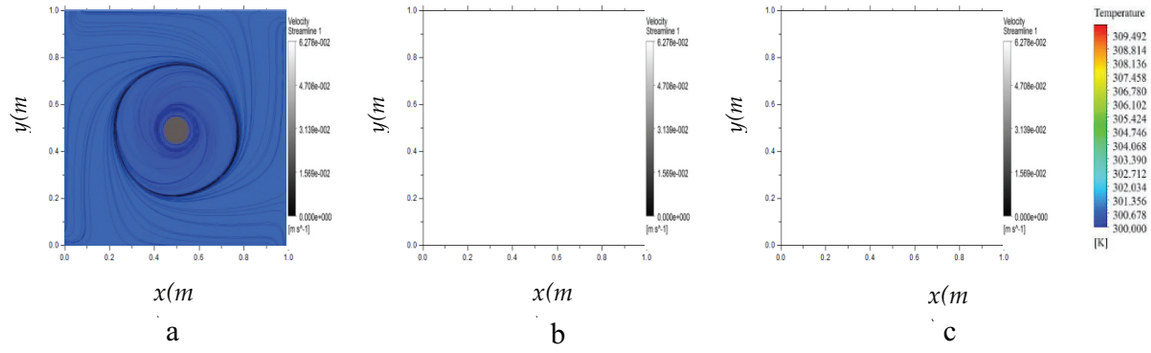

Fig. 15. Results in the horizontal mid plane in the form of temperature contours and stream lines for studied heating conditions, rotation N = 100 rpm: (a) bottom heating, Tb = 310 K , (b) one lateral wall heating, Tp = 310 K, and (c) two lateral walls heating, Te = 310 K.

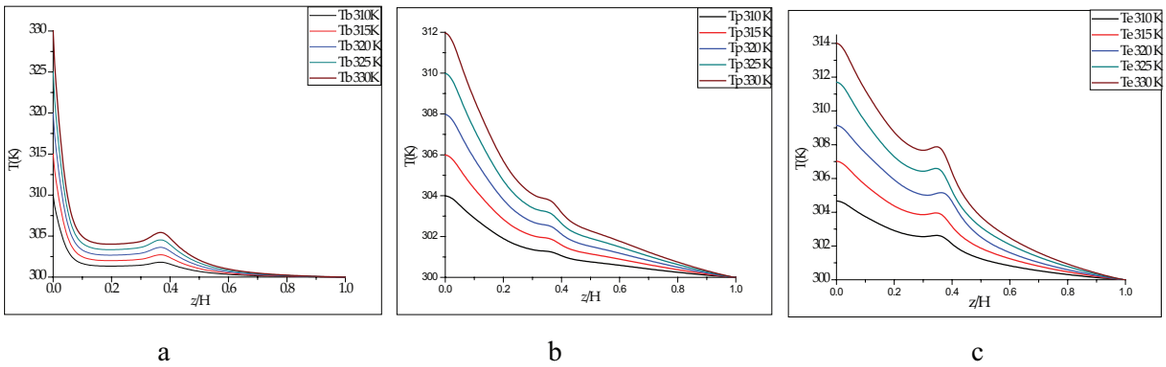

Fig. 16. Temperature profiles in the position x = 0.025 m, N = 100 rpm condition: (a) bottom heating, Tb = 310–330 K, (b) one lateral wall heating, Tp = 310–330 K, and (c) two lateral walls heating, Te = 310–330 K.

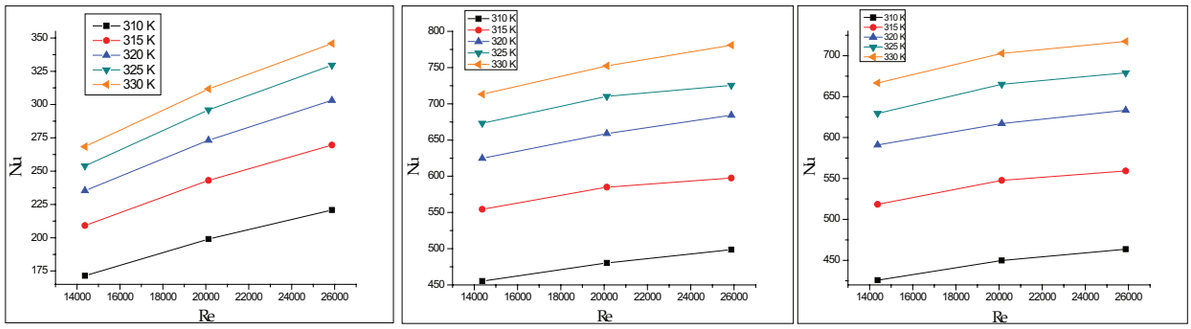

Fig. 17. Nusselt number results at mid-plane, x = 0.1 m, y = 0.05 m, as temperature of heating and Reynolds number increase: (a) bottom heating, *Tb* case, (b) one lateral wall heating, *Tp* case, (c) two lateral walls heating, *Te* case.

5. Conclusions

The rotational movement of water within a square cross section container driven by a centrally placed rotating cylinder was investigated experimental and numerically. The flow patterns are due to pure viscous drag. This configuration was investigated given its potential in a water treatment reactor using UV for disinfection because control of heat and mass transfer is possible. A pair of large-scale vortices, of the kind Taylor-Couette flow, were found for a range of rotation rates under investigation. PIV velocity measurements were made to calculate the turbulence intensity T_u, which was observed to increase in the radial direction towards the corners of the container, as consequence of the interaction fluid-walls. Numerical simulations showed that secondary flows develop in the regions close to the corners, which confirmed the high levels of turbulence found experimentally. Computations of torque were conducted to define the energy consumption. The results indicated that present configuration consumes less energy than a classical concentric-cylinder Taylor-Couette flow. This was attributed to the small size of cylinder used. Heat transfer due to temperature conditions imposed on the walls of the container were analyzed with CFD. It was observed that lateral and bottom heating modifies the vortex motion and structure. Temperature rises to the mid plane and up when heating is imposed on one or two lateral walls. When heating is imposed on the bottom of the container, the Nusselt number rate is smaller compared against heating lateral walls. This result is related to having a suction zone under the rotating cylinder. In summary, Compared to impellers/propellers, a simple cylinder as stirrer has benefits like the generation of vortex motion instead of complex paths. This paper confirms that: first, a square container avoids the use of vertical baffles, which are often implemented in the external cylinder to promote turbulence; second, the use of a simple cylinder as stirrer within a square section container makes it possible to have a controlled vortex motion, which is very important for certain applications like water treatment using UV disinfection. Besides, the use of simple cylinder as a stirrer saves energy, because its consumption is less compared to impellers/propellers; third, turbulence increases in the radial direction due to the presence of corners. This against what is believed that flow in the corners is zero. The numerical simulation demonstrated that ascendant/descendent streams run through the corners.

The results may be useful for a variety of conditions where water treatment or mixing apply, because vortex flows can help controlling residence time and circulation of specific species.

Acknowledgements

Authors from Postgraduate Program at CIICAp recognize and thank the financial support of the National Council for Science and Technology of México, Conacyt, through postgraduate scholarships. Also, grant for project CB-102167-Yby Conacyt was deeply appreciated.

Symbols

D — Diameter of rotating cylinder, m
h_f — Local heat transfer coefficient, W m^{-2} K^{-1}
k_f — Thermal conductivity of fluid, W m^{-1} K^{-1}
N — Rotation rate, rpm
R — Radius of rotating cylinder , m
L — Side wall length of container, m
Nu — Nusselt number,

$$Nu = \frac{qL}{k_f\left(T_w - T_{ref}\right)}$$

q — Heat flux to the wall,

$$q = h_f\left(T_w - T_f\right)$$

T_f — Temperature of fluid, K
T_{ref} — Temperature of reference, K
Tu — Turbulence intensity, $Tu = \frac{\text{rms}}{V} \times 100$, %
T_w — Temperature on the wall, K
rms — Root mean square value of velocity,

$$rms\ \frac{1}{n}\sum_{i=1}^{n}\sqrt{(u_i - \bar{u})^2}\ =, \text{ m s}^{-1}$$

Re — Rotational Reynolds number, $Re = r\omega(L/2\text{-}r)/\nu$
Ta — Taylor number, dimensionless

$\overline{V}, \overline{u}$ — Mean value of velocity magnitude, $\overline{u} = \frac{1}{n}\sum_{i=1}^{n} u_i, ms^{-1}$, m s^{-1}

$\overline{V}_{\tan}$ — Mean value of tangential velocity Component, $\overline{V}_{\tan} = \frac{2\pi Nr}{60}$, m s^{-1}

x, y, z — Cartesian coordinates, m

x_i — Position vector, m

θ — Angle with respect to the tangential coordinate

μ — Dynamic viscosity, kg m^{-1} s^{-1}

ν — Kinematic viscosity, m^{2}s^{-1}

ω — Angular velocity of cylinder, rad s^{-1}

ρ — Density, kg m^{-3}

τ_w — Shear stress at the wall, $\tau_w = \mu \frac{du}{dy}$

References

[1] R.J. Donnelly, Taylor–Couette flow: the early days, Phys. Today, 44 (1991) 32–39.

[2] G.I. Taylor, Stability of a viscous liquid contained between two rotating cylinders, Philos. T. Roy. Soc. A, 223 (1923) 289–343.

[3] R. Tagg, The Couette–Taylor problem, Nonlinear Sci. Today, 4 (1994) 2–25.

[4] H.S. Dou, B. Ch. Khoo, K.S. Yeo, Instability of Taylor–Couette flow between concentric rotating cylinders, Int. J. Therm. Sci., 47 (2008) 1422–1435.

[5] Y.J. Kim, Y.K. Hwang, Experimental study on the vortex flow in a concentric annulus with a rotating inner cylinder, Int. J. KSME, 17 (2003) 562–570.

[6] S. Ch. Tzeng, Heat transfer in a small gap between co-axial rotating cylinders, Int. Commun. Heat. Mass., 33 (2006) 737–743.

[7] V.A.F. Costa, A.M. Raimundo, Steady mixed convection in a differentially heated square enclosure with an active rotating circular cylinder, Int. Commun. Heat Mass, 53 (2010) 1208–1219.

[8] J.S. Kim, D.H. Kim, B. Gu, D.Y. Kim, D.R. Yang, Simulation of Taylor-Couette reactor for particle classification using CFD, J. Cryst. Growth, 373 (2013) 106–110.

[9] I. Recktenwald, N. Alkishriwi, W. Schroder, PIV–LES analysis of channel flow rotating about the streamwise axis, Eur. J. Mech. B-Fluid, 28 (2009) 677–688.

[10] J. Dusting, S. Baladani, Mixing in a Taylor-Couette reactor in the non-wavy flow regime, Chem. Eng. Sci., 64 (2009) 3103–3111.

[11] H. Hartmann, J.J. Derksen, H.E.A. vander Akker, Mixing times in a turbulent stirred tank by means of LES, J. AIChE., 52 (2006) 3696–3706.

[12] A. Paule, B. Lauga, L. Ten-Hage, J. Morchain, R. Moran, E. Paul, J.R. Rols, A photosynthetic rotating annular bioreactor (Taylor-Couette type flow) for phototrophic biofilms cultures, Water Res., 45 (2011) 6107–6118.

[13] G. Muller, G. Newman, W. Weber, Natural convection in vertical Bridgeman configuration, J. Cryst. Growth, 70 (1984) 78–89.

[14] M. Nemri, E. Climent, S. Charton, J.-Y. Lanoë, D. Ode, Experimental and numerical investigation on mixing and axial dispersion in Taylor-Couette flow patterns, Exp. Fluids, 55 (2014) 1769.

[15] S. Lee, C.H. Lee, W.S. Kim, Taylor vortex effect of flocculation of hairy crystals of calcium lactate in anti-solvent crystallization, J. Cryst. Growth, 315 (2012) 32–37.

[16] T.V. Tamhane, J.B. Joshi, U.K. Mudali, R. Natarajan, R.N. Patil, Axial mixing in annular centrifugal extractors, Chem. Eng. J., 207–208 (2012) 462–472.

[17] P. Bonvillani, M.P. Ferrari, E.M. Ducrós, J.A. Orejas, Theoretical and experimental study of the effects of scale-up on mixing time for a stirred-tank bioreactor, Braz. J. Chem. Engi., 23(2006) 1–7.

[18] G. Baier, M.D. Graham, Two-fluid Taylor–Couette flow: experiments and linear theory for immiscible liquids between co-rotating cylinders, Phys. Fluids, 10–12 (1998) 3045–3055.

[19] S.S. Deshmukh, J. B.Joshi, Flow visualization and three-dimensional CFD simulation of the annular region of an annular centrifugal extractor, Ind. Eng. Chem. Res., 47 (2008) 3677–3686.

[20] G. Desmet, H. Verelst, G.V. Baron, Local and global dispersion effects in Couette-Taylor flow-I. Description and modeling of the dispersion effects, Chem. Eng. Sci., 51 (1996) 1287–1298.

[21] S.B. Pawar, B.N. Thorat, CFD simulation of Taylor-Couette flow in scraped surface heat exchanger, Chem. Eng. Res. Des., 90 (2012) 313–322.

[22] M.J. Sathe, S.S. Deshmukh, J.B. Joshi, S.B. Koganti, Computational fluid dynamics simulation and experimental investigation. Study of two-phase liquid-liquid flow in a vertical Taylor-Couette contactor, Ind. Eng. Chem. Res., 49 (2010) 14–28.

[23] T.V. Tamhane, J.B. Joshi, U.K. Mudali, R. Natarajan, R.N. Patil, Measurement of drop size characteristics in annular centrifugal extractors using phase Doppler analyzer (PDPA), Chem. Eng. Res. Des., 90 (2012) 985–997.

[24] S. Vedantam, J.B. Joshi, S.B. Koganti, Three-dimensional CFD simulation of stratified two-fluid Taylor-Couette flow, Can J. Chem. Eng., 84 (2006) 279–288.

[25] T. Imamura, K. Saito, S. Ishikura, A new approach to continuous emulsion polymerization, Poly Int., 30 (1993) 203–206.

[26] T. Ogihara, G. Matsuda, T. Yanagawa, N. Ogata, K. Fujita, M. Nomura, Continuous synthesis of mono dispersed silica particles using Couette-Taylor vortex flow, J. Cer. Soc. Jpn. Int., 103 (1995) 151.

[27] W.S. Kim, Application of Taylor vortex to crystallization, J. Chem. Eng. Jpn., 47 (2014) 115–123.

[28] S. Cohen, M.D. Moalem, Analysis of a rotating annular reactor in the vortex flow regime, Chem. Eng Sci., 46 (1991) 123–134.

[29] S. Poncet, S. Haddadi, S. Viazzo, Numerical modeling of fluid flow and heat transfer in a narrow Taylor-Couette-Poiseuille system, Int. J. Heat Fluid Flow, 32 (2011) 128–144.

[30] B. Kumar, Energy dissipation and shear rate with geometry of baffled surface aerator, Chem. Eng. Res. Bull., 14 (2010) 92–96.

[31] C. Wylock, V. Gutierrez, F. Debaste, T. Cartage, M.P. Delplancke-Ogletree, B. Haut, Influence of mixing and solid concentration on sodium bicarbonate secondary nucleation rate in stirred tank: theoretical and experimental studies, Crys. Res. Tech., 45 (2010) 929–938.

[32] J.J. Derksen, K. Kontomaris, J.B. McLaughlin, H.E.A. van den Akker, Large-eddy simulation of single-phase flow dynamics and mixing in an industrial crystallizer, Trans. IChemE, Part A, Chem. Eng. Res. Des., 85 (2007) 169–179.

[33] A. Bakker, J.B. Fasano, Time dependent, turbulent mixing and chemical reaction in stirred tanks, AIChE Sym. Series, 299 (1993) 71–78.

[34] J.G. Sczechowski, C.A. Koval, R.D. Noble, A Taylor vortex reactor for heterogeneous photo-catalysis, Chem. Eng. Sci., 50 (1995) 3163–3173.

[35] A.R. Rao, B. Kumar, Scale-up criteria of square tank surface aerator, Biotech. Bioeng., 96 (2007) 464–470.

[36] W. Chtourou, M. Ammar, Z. Driss, M.S. Abid, CFD prediction of the turbulent flow generated in stirred square tank by a Rushton turbine, Ener. Power Eng., 6 (2014) 95–110.

[37] J. Kilander, S. Blomström, A. Rasmuson, Scale-up behavior in stirred square flocculation tanks, Chem. Eng. Sci., 62 (2007) 1606–1618.

[38] J. Kilander, S. Blomström, A. Rasmuson, Spatial and temporal evolution of floc size distribution in a stirred square tank investigated using PIV and image analysis, Chem. Eng. Sci., 61 (2006) 7651–7667.

[39] J. Kilander, F.J.E. Svensson, A. Rasmuson, Flow instabilities, energy levels, and structure in stirred tanks, AIChE., 52 (2006) 4039–4051.

[40] J. Kilander, A. Rasmuson, Energy dissipation and macro instabilities in a stirred square tank investigated using an LEPIV approach and LDA measurements, Chem. Eng. Sci., 60 (2005) 6844–6856.

[41] A.R. Rao, Prediction of reaeration rates in square, stirred tanks, J. Env. Eng., 125(1999) 215–223.

[42] R.D. Keane, R.J. Adrian, Theory of cross-correlation analysis of PIV Images, J. App. Sci. Res., 49(1992) 1–27.
[43] M.K. Shah, M. Agelinchaab, M.F. Tachie, Influence of PIV interrogation area on turbulent statistics up to 4th order moments in smooth and rough wall turbulent flows, Int. J. Exp. Thermal Fluid Sc., 32 (2008) 725–747.
[44] B. Ganapathisubramani, E.K. Longmire, I. Marusic, S. Pophos, Dual-plane PIV technique to determine the complete velocity gradient in a turbulent boundary layer, Exp. Fluids, 39 (2005) 222–231.
[45] J. Westerweel, On velocity gradients in PIV interrogation, Exp. Fluids, 44 (2008) 831–842.
[46] M. Piirto, P. Saarenrinne, H. Eloranta, R. Karvinen, Measuring turbulence energy with PIV in backward-facing step flow, Exp. Fluids, 35 (2003) 219–236.
[47] Dantec Dynamics Inc.: Particle Image Velocimetry System Flow Manager, User's guide: Tonsbakken Ed., Skovlunde, 2009.
[48] H.W. Coleman, W.G. Steele, Experimentation and Uncertainty Analysis for Engineers: John Wiley, New York, 1989.
[49] J. Forliti, P.J. Strykowski, K. Debatin, Bias and precision errors of digital particle image velocimetry, Exp. Fluids, 28 (2000) 436–447.
[50] S. Lee, A. Choi, W.S. Kim, A.S. Myerson, Phase transformation of sulfamerazine using a Taylor vortex, J. Cryst. Growth Des., 11 (2011) 5019–5029.
[51] M. Nemri, E. Climent, S. Charton, J.Y. Lanoë, D. Ode, Experimental and numerical investigation on mixing and axial dispersion in Taylor-Couette flow patterns, Chem. Eng. Res. Des., 9 (2013) 2346–2354.
[52] A. Racina, M. Kind, Specific power input and local micromixing times in turbulent Taylor-Couette flow, Exp. Fluids, 41 (2006) 513–522.
[53] W.D. McComb: The physics of fluid turbulence, Oxford Univ. Press, New York, 1994.
[54] R. van Hout, J. Kats, Measurements of mean low and turbulence characteristics in high-Reynolds number counter-rotating Taylor-Couette flow, Phys. Fluids, 23 (2011) 105102–11.
[55] Fluent Inc.: Fluent V6.2 User's Guide, Vol. 3, Canterra Resource Park, 10 Cavendish Court, Lebanon NH, 2010.